


## Effect of electric and chiral magnetic conductivities on azimuthally fluctuating electromagnetic fields and observables in isobar collisions

Irfan Siddique<sup>1,\*</sup> and Uzma Tabassam<sup>2</sup>

<sup>1</sup>*School of Nuclear Science and Technology, University of Chinese Academy of Sciences, Beijing 101408, China*

<sup>2</sup>*Department of Physics, COMSATS University Islamabad Campus, Islamabad, Park Road, 44000, Pakistan*

 (Received 19 October 2023; revised 22 December 2023; accepted 26 January 2024; published 8 March 2024)

We study the space-time evolution of electromagnetic fields along with the azimuthal fluctuations of these fields and their correlation with the initial matter geometry specified by the participant plane in the presence of finite electric ( $\sigma$ ) and chiral magnetic ( $\sigma_\gamma$ ) conductivities in Ru + Ru and Zr + Zr collisions at  $\sqrt{s_{NN}} = 200$  GeV. We observe the partially asymmetric behavior of the spatial distributions of the electric and magnetic fields in a conducting medium when compared to the Lienard-Wiechert (L-W) solutions, and deceleration of the decay of the fields is observed in both isobar collisions. While studying the correlation between the magnetic field direction and the participant plane, we see the sizeable suppression of the correlation in the presence of finite conductivities when compared to the L-W case, reflecting the importance of taking into account the medium properties such as conductivities while calculating the magnetic field induced observable quantities.

DOI: [10.1103/PhysRevC.109.034905](https://doi.org/10.1103/PhysRevC.109.034905)

### I. INTRODUCTION

The ultrarelativistic heavy ion collision creates a deconfined state with extremely high energy and density known as quark-gluon plasma (QGP). In noncentral heavy ion collisions, along with this high energy and density state, very strong electromagnetic fields are also generated due to charged particles having relativistic motions, which provides an opportunity to study related phenomenon in heavy ion collisions. Typical strength of the magnetic field produced in heavy ion collisions can be estimated in co-moving frame for fast moving nuclei by  $eB \sim \gamma Ze^2/R_A^2$  with  $\gamma$  being the Lorentz factor,  $Z$  being the proton number, and  $R_A$  being the radius of the nucleus. For the case of Au + Au collisions at top BNL Relativistic Heavy Ion Collider (RHIC) energies ( $\sqrt{s_{NN}} = 200$  GeV) the magnetic field is of orders of  $eB \sim m_\pi^2 \approx 10^{18}$  Gauss [1–3] and these fields are proportional to collision energy so at CERN Large Hadron Collider (LHC) energies in Pb + Pb collisions at ( $\sqrt{s_{NN}} = 2.76$  TeV) it can be roughly 10 times stronger [4,5]. In recent years, many developments and efforts have been made to explore the effects induced by (electro)magnetic fields such as the chiral magnetic effect (CME) [6–11], the chiral separation effects (CSE) [12,13], chiral magnetic wave (CMW) [14–18], etc. All of these effects are related to chiral fermions or massless fermions. Search for the CME is currently a very active field of interest in heavy ion collisions at the RHIC and LHC [19–25]. In early STAR and ALICE experiments, the charge separation effect was measured by measuring two particle azimuthal angle correlation  $\gamma_{\alpha\beta} = \langle \cos(\phi_\alpha + \phi_\beta - 2\Psi_{RP}) \rangle$  with  $\phi_i$  being the azimuthal angle of corresponding charged particle,  $\alpha$  ( $\beta$ ) denotes the sign of charge particle (either positive

or negative), and  $\Psi_{RP}$  being the reaction plane angle, and the measurements support the presence of CME [19–21]. But due to inseparable contribution from the background, it is extremely difficult to properly understand and extract the CME signal from the huge background in experiment results [23,25–28]. There have been several attempts to eliminate or reduce background effects [29–32].

According to the expectations from CME, the difference between the correlation of opposite charge pairs ( $\gamma_{\text{opposite}}$ ) and same charge pairs ( $\gamma_{\text{same}}$ ) is expected to be directly proportional to the strength of the squared magnetic field ( $e\mathbf{B}$ )<sup>2</sup> and azimuthal fluctuations of the magnetic field direction ( $\cos 2(\Psi_B - \Psi_2)$ ) [33–35], i.e.,

$$\Delta\gamma = \gamma_{\text{opposite}} - \gamma_{\text{same}} \propto \langle (e\mathbf{B})^2 \cos 2(\Psi_B - \Psi_2) \rangle, \quad (1)$$

where  $\Psi_B$  represents the azimuthal angle of the magnetic field and  $\Psi_2$  represents the second harmonic participant plane angle. The right hand side of the above equation shows that the quantitative contribution of the B-field-induced effect is essentially controlled by  $(e\mathbf{B})^2 \cos 2(\Psi_B - \Psi_2)$ , therefore this projected field strength controls the contribution rather than  $(e\mathbf{B})^2$  alone.

To extract the CME signal, a solution proposed is to carry out isobaric collisions  $\text{Ru}_{44}^{96} + \text{Ru}_{44}^{96}$  (Ru: ruthenium) and  $\text{Zr}_{40}^{96} + \text{Zr}_{40}^{96}$  (Zr: zirconium) [36] and experiments were performed at RHIC [37–39] along this line to observe these effects. These isobaric collisions are intensely pursued for investigation because the advantage is that the difference in number of protons can generate different magnitudes of the electromagnetic fields and related induced effects, but the same mass number in two isobar systems can generate the same background effect. So one can expect to observe the CME signal if it really exists in heavy ion collisions. For instance, from Woods-Saxon distributions it can be confirmed that in isobaric collisions  $e\mathbf{B}$  differs by 10% [40], which

\*irfansiddique@ucas.ac.cn

naively agrees with the fact that the atomic number in Ru and Zr differ by 10% (Ru-44, Zr-40), so there can be a chance of observing a CME signal according to Eq. (1). There are several studies that show the framework to search for CME and predict the correlation observables by using the initial magnetic field produced in isobar collisions, i.e., introducing the initial charge separation proportional to magnetic field in a multiphase transport (AMPT) model and studying the effect of final state interactions on CME observables [41], detecting CME signal, and predicting the correlation observables by using absolute difference between two isobars event with identical multiplicity and elliptic flow in anomalous-viscous fluid dynamics (AVFD) framework [42], measurement of  $\Delta\gamma$  with respect to reaction plane ( $\Psi_{RP}$ ) and participant plane ( $\Psi_{pp}$ ) and compare between them by using the Monte Carlo (MC) Glauber and AMPT models [31], reflecting information about CME by studying the correlation between (initial) magnetic field direction and second harmonics of participant plane angle  $\Psi_{pp}$  (and spectator plane  $\Psi_{sp}$ ) [43]. In previous studies, magnetic field without medium feedback is used for making predictions about CME and correlation observables however in this study we follow [43] and perform analysis for a more realistic nuclear matter that take into account medium feedback in terms of electric and chiral magnetic conductivities.

Supposing that two isobar systems have the same background, then  $\Delta\gamma$  is expecting main contributions from the squared magnetic field and the correlation between the azimuthal angle of the magnetic field  $\Psi_B$  and participant plane  $\Psi_2$ . So the first key ingredient is the fact that a magnetic field, whose spatial and time evolution in different mediums can behave differently [44–49], consequently can have an effect on related observables. The chiral conductivity being directly proportional to the chiral chemical potential fluctuates in each event. When computing event-averaged observables, the intrinsic diversity in the chiral chemical potential for each event presents a difficulty in directly determining its impact on the observable. However, in the context of event-by-event analysis, each unique event contains the distinct influence of the chiral conductivity on the observable. In contrast to the case where fluctuations are averaged out over several events, the event-by-event analysis enables us to capture and study the subtle influence of variations in the chiral chemical potential on the observable. Although it is difficult to see the direct influence of the chiral chemical potential while calculating event-averaged observable, in event-by-event analysis each event encodes its effect in calculating the observable so its effect is not totally smoothed out. In this paper, we will look at the electric and magnetic fields produced in isobar collisions in the presence of electric and chiral magnetic conductivities and measure their effect on the azimuthal fluctuations of the electromagnetic fields and related observable quantities.

After providing the brief introduction, in Sec. II we give the expressions for electric and magnetic fields in a zero conductivity system and system having finite conductivity. In Sec. III, we provide simulation results and discussions for the electromagnetic fields and their correlation with initial matter geometry specified by the participant plane in central and noncentral isobaric collisions. Finally we summarize in Sec. IV.

## II. CALCULATION OF ELECTROMAGNETIC FIELD

### A. Zero-conductivity system ( $\sigma = \sigma_\chi = 0$ )

For a system with zero conductivity, or vacuum ( $\sigma = \sigma_\chi = 0$ ), the electric and magnetic field in each event can be evaluated by using the Lienard-Wiechert potential [1,33] as

$$\mathbf{E}(t, \mathbf{x}) = \alpha_{EM} \sum_n \frac{(1 - v_n^2) \mathbf{R}_n}{(\mathbf{R}_n^2 - (\mathbf{R}_n \times \mathbf{v}_n)^2)^{3/2}}, \quad (2)$$

$$\mathbf{B}(t, \mathbf{x}) = \alpha_{EM} \sum_n \frac{(1 - v_n^2)(\mathbf{v}_n \times \mathbf{R}_n)}{(\mathbf{R}_n^2 - (\mathbf{R}_n \times \mathbf{v}_n)^2)^{3/2}}, \quad (3)$$

where  $\mathbf{R}_n = \mathbf{x} - \mathbf{x}_n$  is the relative position vector between the source point  $\mathbf{x}_n$  and the field point  $\mathbf{x}$  under discussion, and  $\mathbf{x}_n$  and  $\mathbf{v}_n$  represent the position and velocity, respectively, of the  $n$ th proton in the colliding nuclei at the current time  $t$ . In the above equation  $\alpha_{EM} = e/4\pi \approx 1/137$  is the fine structure constant. Note that Eqs. (2) and (3) are valid under the assumption that all the source charges are traveling with a constant velocity. If all the charges do not have constant velocity then the original form of the Lienard-Wiechert fields [2,48] using the retarded time should be used for the calculation of the electric and magnetic fields.

### B. Conducting system with finite conductivities ( $\sigma \neq 0, \sigma_\chi \neq 0$ )

The quark-gluon plasma (QGP) matter is produced in heavy-ion collisions and due to its certain conducting property, it is important to take into account the feedback effects of the conductivities. The Maxwell equations with both electric ( $\sigma$ ) and chiral magnetic ( $\sigma_\chi$ ) conductivities can be written in the following form:

$$\nabla \cdot \mathbf{F} = \begin{cases} \rho_{\text{ext}}/\epsilon & \rightarrow \mathbf{E} \\ 0 & \rightarrow \mathbf{B} \end{cases}, \quad (4)$$

$$\nabla \times \mathbf{F} = \begin{cases} -\partial_t \mathbf{B} & \rightarrow \mathbf{E} \\ \partial_t \mathbf{E} + \mathbf{J}_3(\sigma, \sigma_\chi) & \rightarrow \mathbf{B} \end{cases}, \quad (5)$$

where  $\rho_{\text{ext}}$  is the external charge density and  $\mathbf{J}_3(\sigma, \sigma_\chi) = \mathbf{J}_{\text{ext}} + \sigma \mathbf{E} + \sigma_\chi \mathbf{B}$  with  $\mathbf{J}_{\text{ext}}$  being the external current density,  $\sigma \mathbf{E}$  being the electric current, and  $\sigma_\chi \mathbf{B}$  the being chiral current, and  $\mathbf{F}$  denotes either electric ( $\mathbf{E}$ ) or magnetic ( $\mathbf{B}$ ) field. We can obtain the following algebraic expressions for the electric and magnetic field components with finite electric and chiral conductivity by solving the above Maxwell equation using the Green's function method in cylindrical coordinates by considering that all source charges fly along the  $z$  axis [47]:

$$\begin{aligned} B_\phi(t, \mathbf{x}) &= \frac{Q}{4\pi} \frac{v\gamma x_T}{\Delta^{3/2}} \left( 1 + \frac{\sigma v\gamma}{2} \sqrt{\Delta} \right) e^A, \\ B_r(t, \mathbf{x}) &= -\sigma_\chi \frac{Q}{8\pi} \frac{v\gamma^2 x_T}{\Delta^{3/2}} e^A \left[ \gamma(vt - z) + A\sqrt{\Delta} \right], \\ B_z(t, \mathbf{x}) &= \sigma_\chi \frac{Q}{8\pi} \frac{v\gamma}{\Delta^{3/2}} e^A \left[ \Delta \left( 1 - \frac{\sigma v\gamma}{2} \sqrt{\Delta} \right) \right. \\ &\quad \left. + \gamma^2 (vt - z)^2 \left( 1 + \frac{\sigma v\gamma}{2} \sqrt{\Delta} \right) \right], \end{aligned} \quad (6)$$

in which  $\Delta$  is defined as  $\Delta \equiv \gamma^2(vt - z)^2 + x_T^2$  and  $A$  is defined as  $A \equiv (\sigma v \gamma / 2)[\gamma(vt - z) - \sqrt{\Delta}]$ ; and

$$\begin{aligned}
 E_\phi(t, \mathbf{x}) &= \sigma_\chi \frac{Q}{8\pi} \frac{v^2 \gamma^2 x_T}{\Delta^{3/2}} e^A [\gamma(vt - z) + A\sqrt{\Delta}], \\
 E_r(t, \mathbf{x}) &= \frac{Q}{4\pi} e^A \left\{ \frac{\gamma x_T}{\Delta^{3/2}} \left( 1 + \frac{\sigma v \gamma}{2} \sqrt{\Delta} \right) \right. \\
 &\quad \left. - \frac{\sigma}{v x_T} e^{-\sigma(t-z/v)} \left[ 1 + \frac{\gamma(vt - z)}{\sqrt{\Delta}} \right] \right\}, \\
 E_z(t, \mathbf{x}) &= \frac{Q}{4\pi} \left\{ -\frac{e^A}{\Delta^{3/2}} \left[ \gamma(vt - z) + A\sqrt{\Delta} + \frac{\sigma \gamma}{v} \Delta \right] \right. \\
 &\quad \left. + \frac{\sigma^2}{v^2} e^{-\sigma(t-z/v)} \Gamma(0, -A) \right\}, \quad (7)
 \end{aligned}$$

where  $\Gamma(0, -A)$  is an incomplete gamma function defined as  $\Gamma(a, z) = \int_z^\infty t^{a-1} \exp(-t) dt$ . It can be verified that with zero conductivity limit, Eqs. (6) and (7) return to the Lienard-Wiechert solution.

We have used the MC Glauber model developed by the PHOBOS collaboration [50] to calculate the spatial distribution of the source nucleons. The MC Glauber models are useful for estimating electromagnetic (EM) fields in heavy ion collisions, and also with the help of Glauber model computations we can connect experimental data to a collision centrality and other geometric quantities such as eccentricity, initial state anisotropy, etc. [49,51–53]. To determine the spatial information of the source charges, a two-step calculation is performed in this model. The reaction plane is defined by the impact parameter and the beam direction, represented by the  $x$  axis and  $z$  axis, respectively. First, the centers of projectile and target nuclei are located at  $x = \pm b/2$  for a given impact parameter  $b$ , and then it is employed to determine the spatial positions of nucleons stochastically in the two colliding nuclei. The density profile of isobar nucleus has the following Woods-Saxon (WS) distribution

$$\rho(x, y, z) = \frac{\rho_0}{1 + \exp\left[\frac{r - R(1 + \beta_2 Y_{20} + \beta_4 Y_{40})}{f}\right]}, \quad (8)$$

where  $\rho_0$  is the nuclear density at the nucleus center,  $f$  represents the surface thickness parameter, and  $Y_{nl}(\theta)$  represents the spherical harmonic functions. Here,  $\beta_2$ , and  $\beta_4$  are deformation parameters and they determine the deviation from a spherical shape of the nucleus. Taking into account these parameters allows us to obtain more realistic representations of the spatial distribution of nucleons within the projectile and target nuclei. After determining the Woods-Saxon distribution information, the subsequent motions are then assumed to be along straight trajectories in the beam direction (i.e., in  $+/-z$  directions). The collision between nucleons from the projectile and target nucleus occurs if they satisfy  $d \leq \sqrt{\sigma_{\text{inel}}^{NN}/\pi}$ , where  $d$  is the distance in the transverse plane and  $\sigma_{\text{inel}}^{NN}$  denotes the inelastic cross section of nucleon-nucleon collisions. Those nucleons that do not partake in collisions are labeled as “spectators” while those that partake in collisions are labeled as “participants”.

TABLE I. Woods-Saxon parameters for Ru and Zr.

Deformed nuclei case [54–56]			
	$R_0$	$a$	$\beta_2$
Ru	5.085	0.46	0.158
Zr	5.020	0.46	0.08
Halo-type nuclei case [57,58]			
Ru, $n$	5.085	0.523	0
Ru, $p$	5.085	0.523	0
Zr, $n$	5.021	0.592	0
Zr, $p$	5.021	0.523	0

In this work, we have used two isobar systems, i.e.,  $^{96}_{44}\text{Ru} + ^{96}_{44}\text{Ru}$  (ruthenium-96) and  $^{96}_{40}\text{Zr} + ^{96}_{40}\text{Zr}$  (zirconium-96) collisions. There are several WS parameter settings for two isobar nuclei. For the case of the deformed nuclei structure, we use  $R = 5.085$  fm and 5.020 fm for Ru and Zr, respectively, and  $d = 0.46$  fm for both isobar collisions at  $\sqrt{s_{NN}} = 200$  GeV. The deformation parameter  $\beta_2$  is not confirmed yet and there are two cases for  $\beta_2$  [54–56]. In one situation the deformation parameter for  $^{96}_{44}\text{Ru}$  is larger than  $^{96}_{40}\text{Zr}$  ( $\beta_2^{\text{Ru}} = 0.158$  and  $\beta_2^{\text{Zr}} = 0.08$ ), while in other situation the deformation parameter for  $^{96}_{44}\text{Ru}$  is smaller than  $^{96}_{40}\text{Zr}$  ( $\beta_2^{\text{Ru}} = 0.053$  and  $\beta_2^{\text{Zr}} = 0.217$ ). In this paper we have only considered the first situation because the effect of the deformation parameter has been studied in Ref. [43]. Apart from the deformed nuclei structure there are also other WS distributions which can reflect neutron-skin effect, details of these parameter settings and effects are given and studied in [57,58]. Among several WS parameter settings studied in [58], the halo-type nuclei have reproduced best experimental results for average numbers of charge particles, charged particle multiplicity ( $N_{\text{ch}}$ ), and elliptical flow so we also considered the halo-type nuclei structure along with the deformed nuclei structure. WS parameters used in this study are given in Table I.

In Fig. 1, we show our initial charge distribution based on the Phobos MC Glauber model on the three-dimensional (3D) plane together with their XZ projections on the XY plane for  $^{96}_{40}\text{Ru} + ^{96}_{40}\text{Ru}$  at  $b = 7$  fm. Solid blue and green circles represent participant nucleons from the two colliding nuclei, while red and magenta open circles represent spectators that do not participate in inelastic scatterings. In order to assess whether a nucleon (proton) contributes to the electromagnetic field, we utilize the probability  $Z/A$  (44/96 for the Ru nucleus and 40/96 for the Zr nucleus). The evaluation of the electromagnetic field takes into account the contributions from the protons in both participants and spectators. It has been found that there is a tiny difference in magnitudes between considering only spectators and all nucleons. For instance, in Ru + Ru collisions at  $b = 9$  fm, protons in the spectator alone produce around 4% less  $B_y$  than protons in the entire nucleus and almost similar yield is observed as well for Zr + Zr collisions in our setup. For calculating the electromagnetic fields in the rest of this study, we perform event-by-event analysis over  $10^5$  MC Glauber events for each impact parameter (number

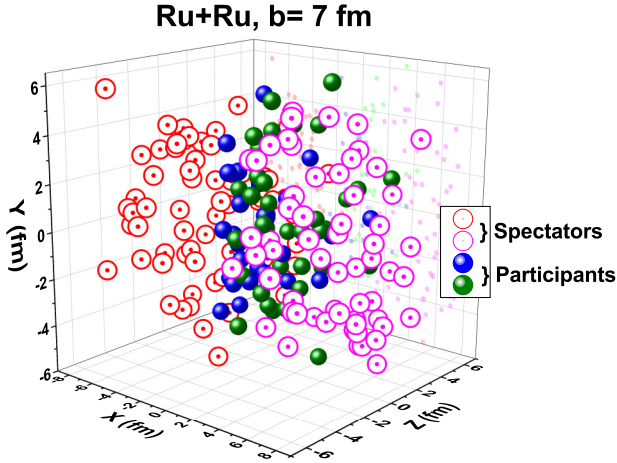


FIG. 1. Initial geometry of a Ru + Ru collision event generated by the MC Glauber model for  $b = 7$  fm and  $\sqrt{s_{NN}} = 200$  GeV into the 3D plane.

of participants) setup to obtain an event-by-event geometric distribution of the source charges and relevant results.

The main objective is to study the correlation between the electromagnetic fields and plane angle formed by participants for zero-conductivity and finite conductivity cases, we use the definition of the  $n$ th plane participant plane angle represented by  $\Psi_n$  which can be calculated as

$$\Psi_n = \frac{\text{atan2}(\langle r_p^2 \sin(n\phi_p) \rangle, \langle r_p^2 \cos(n\phi_p) \rangle) + \pi}{n}, \quad (9)$$

where  $n$  can be 1, 2, 3... representing different flow harmonics, however, in this work we only consider  $n = 2$  because the second harmonics are most prominent and are tightly correlated to the initial geometry distributions,  $r_p$  represents the displacement of participating nucleons from the field point  $\mathbf{r}$ , and  $\phi_p$  represents their corresponding azimuthal angle on the transverse plane. We also check the similarity and dissimilarity between zero-conductivity limit and finite conductivity system by calculating relative ratios defined by

$$X_c = 2 \frac{c^{Ru} - c^{Zr}}{c^{Ru} + c^{Zr}}, \quad (10)$$

where  $c$  represents correlation  $\langle \cos 2(\Psi_F - \Psi_2) \rangle$  or  $\langle e\mathbf{F}^2 \cos 2(\Psi_F - \Psi_2) \rangle$  in our calculations.  $X_c$  close to zero represents similarity while away from zero represents dissimilarity between two isobar collision systems. Also by studying relative ratio trends we can get information about the qualitative difference in the zero-conductivity case and finite conductivities case. If trends differ from each other more it will show a difference in qualitative behavior in the vacuum scenario and finite conductivity scenario.

### III. SIMULATION RESULTS AND DISCUSSIONS

#### A. Effects on electromagnetic fields

##### 1. Spatial distributions

In this subsection we show the numerical results of the contour plots of the electric and magnetic fields compared

between the zero-conducting system and finite conductivity system (which have finite values of electric and chiral magnetic conductivity) for isobar collisions. As described in the previous section, the space-time evolution profile for electric charges for Ru + Ru and Zr + Zr is used for collisions at  $\sqrt{s_{NN}} = 200$  GeV for different impact parameters. We use the Lienard-Wiechert solution for the case of zero conductivity ( $\sigma = \sigma_\chi = 0$ ), while for finite conductivity case Maxwell equations are solved to obtain the electromagnetic fields.

In Figs. 2 and 3, we show the contour plots of the magnetic field  $\langle B_{x,y,z} \rangle$  and electric field  $\langle E_{x,y,z} \rangle$  in Ru + Ru collisions for  $b = 7$  fm at  $\sqrt{s_{NN}} = 200$  GeV. Each figure consists of two rows, in the first row results from Lienard-Wiechert solution for zero-conductivity case are presented and in the second row results in the presence of finite conductivities are presented. In our simulation for the case of finite conductivities, we take the values of conductivities as  $\sigma = 5.8$  MeV and  $\sigma_\chi = 1.5$  MeV, the same as Refs. [47,49]. Here, we notify that  $\sigma = 5.8$  MeV is consistent to the lattice quantum chromodynamics calculations at top temperature of QGP produced at RHIC and it is expected that the expansion of QGP causes the decrease in  $\sigma$  together with the temperature of medium. Currently there is no direct estimation towards choosing the  $\sigma_\chi$ . Since the analytic solutions of Maxwell equations for the electric and magnetic fields given in Eqs. (6) and (7) are obtained under the condition  $\sigma \gg \sigma_\chi$  in Ref. [47], we take  $\sigma_\chi = 1.5$  MeV as taken in the earlier work. The snapshot for zero-conductivity case is presented at  $t = 0$  fm/c in the first row while the snapshot for the finite conductivities case is presented at  $t = t_Q$  fm/c in the second row for the Ru + Ru collision at  $b = 7$  fm at  $\sqrt{s_{NN}} = 200$  GeV. We choose  $t = t_Q$  fm/c for the finite conductivity case because we observed a maximum strength of field at this time as will be shown in Sec. III A 3. One can notice that spatial distributions of the electric and magnetic fields around  $x = 0$  and  $y = 0$  axes are symmetric when  $\sigma = \sigma_\chi = 0$ . Once we have finite conductivities then the symmetry of spatial distribution for the electric and magnetic fields is broken, that is they appear symmetric around the  $x = 0$  axis but asymmetric around the  $y = 0$  axis. This is due to the presence of  $\sigma_\chi$  in  $E_\phi$  and  $B_r$  in the electric field and magnetic field, respectively. More details about broken symmetry of spatial distribution of the electric and magnetic fields are given in Refs. [47,49]. We have also checked the spatial distribution for Zr + Zr collisions at  $b = 7$  fm at  $\sqrt{s_{NN}} = 200$  GeV and found that the trends for both cases are similar to those in Ru + Ru collisions.

#### 2. Centrality dependence

In this subsection we present the centrality dependence for the electric and magnetic fields in the vacuum case and the finite conductivity case and show a comparison between them. Shown in Fig. 4 are the results for different impact parameters from central to noncentral Ru + Ru collisions with two different WS parameters for the vacuum (left panel) and finite conductivities cases (right panel). Solid symbols with solid lines represent results for the halo-type WS parameters while open symbols with dashed lines are for the deformed nuclei WS parameters for Ru in Ru + Ru collisions. Results



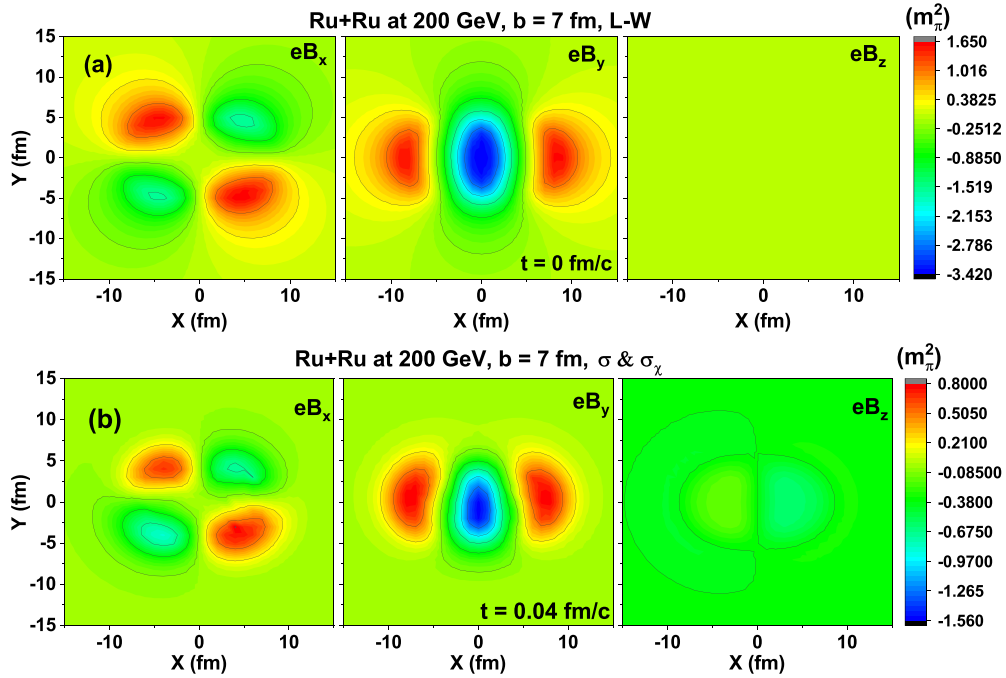


FIG. 2. Spatial distribution of a magnetic field components ( $eB_{x,y,z}$  in units of  $m_\pi^2$ ) in Ru + Ru for  $b = 7$  fm at  $\sqrt{s_{NN}} = 200$  GeV, compared between zero conductivity case (first row) vs finite conductivities case (second row).

show very little difference when the impact parameter is large but for small impact parameter almost no difference is found.

Shown in Fig. 5 are the results for different impact parameters from central to noncentral collisions with halo-type structure of Ru and Zr. Solid symbols with solid lines represent results from Ru + Ru collisions while open symbols with

dashed lines are results from Zr + Zr collisions. Clearly one can see that the impact parameter plays an important role on the strength of the electric and magnetic field components. For the case of zero conductivity as shown in Fig. 5(a) the results are similar to the results of electromagnetic fields for Au + Au and isobar collisions as in Refs. [1,2] and [43],

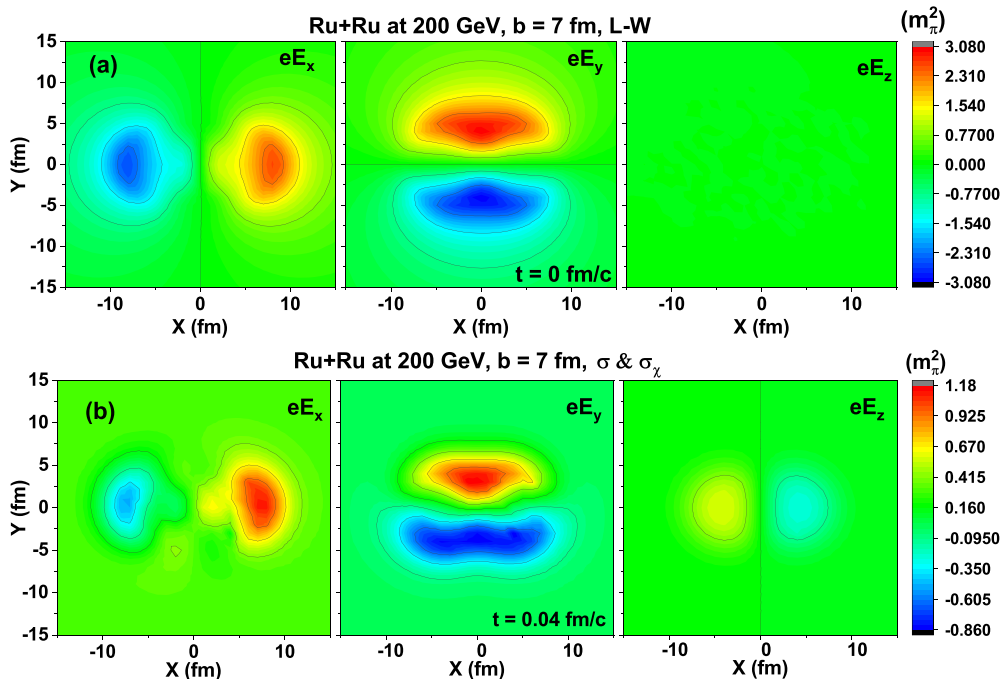


FIG. 3. Spatial distribution of a electric field components ( $eE_{x,y,z}$  in unit of  $m_\pi^2$ ) in Ru + Ru for  $b = 7$  fm at  $\sqrt{s_{NN}} = 200$  GeV, compared between zero conductivity case (first row) vs finite conductivities case (second row).

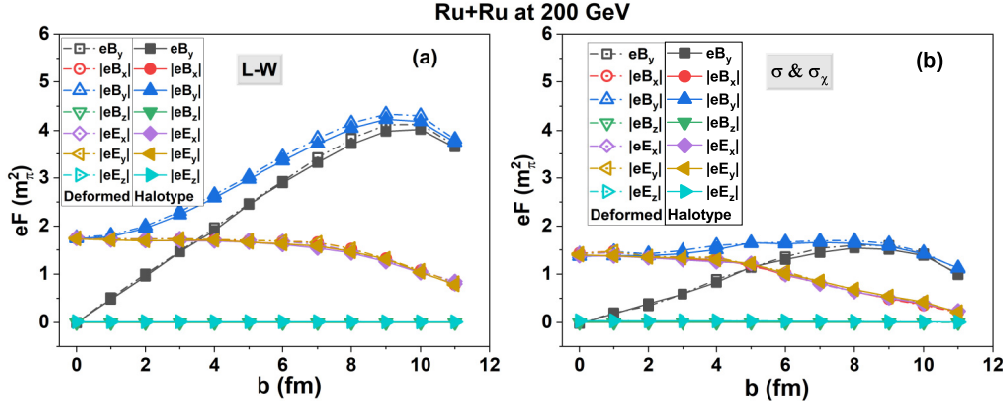


FIG. 4. Comparison between  $e\mathbf{F}(m_\pi^2)$  for deformed (open symbols) and halo-type (closed symbols) nuclei structure for Ru + Ru collision at  $\sqrt{s} = 200$  GeV.

respectively. Moreover, the magnitudes of the magnetic and electric fields ( $e\mathbf{F}$ ) follow  $e\mathbf{F}_{Au} > e\mathbf{F}_{Ru} > e\mathbf{F}_{Zr}$  because of the decreasing number of protons in three collision systems, respectively. Note that our simulation results show  $|eB_x| \approx |eE_x| \approx |eE_y|$ . For the case of finite conductivities as shown in Fig. 5(b), we present the impact parameter dependence of the electric and magnetic field components at time  $t_Q$ . We clearly see that the presence of conductivities suppresses the strength significantly for  $eB_y$  and  $|eB_y|$ , however the magnitudes for  $|eB_x|$  and  $|eE_{x,y}|$  are still comparable in the vacuum and finite conductivity cases for small impact parameters. The longitudinal components of the electric and magnetic field  $eF_z$  are always much smaller and consistent to zero in comparison with transverse components for both vacuum and finite conductivity cases.

### 3. Time evolution

In this subsection we show the time evolution of electric and magnetic fields in vacuum and finite-conductivities systems and show comparison between them. Since the dominant component is the magnetic field perpendicular to the reaction plane so in Fig. 6 we show the time evolution of  $eB_y$  in units of  $m_\pi^2$  for isobar collisions in the log-scale. From the figure, we

can see that for both isobar collisions although the magnitude for the vacuum case is large as compared to the conducting medium case at the beginning but the former damps faster than the latter. From the figure we also see that in the case of conductivities, time evolution has a peak and reaches its maximum at  $t_Q \approx 0.05$  (0.03) fm/c for  $b = 8$  (4) fm in our calculations. So all the results which we present in this paper for the case of conductivities are at  $t = t_Q$  fm/c because the maximum strength of the field is achieved at this time. We also see that simulation results of Zr + Zr collisions are smaller as compared to Ru + Ru collisions due to less number of protons. We also compare the ratio  $eB_y(Ru)/eB_y(Zr)$  in the bottom of the figure from Ru to Zr in two cases and they are around 1.1 consistent with the ratios of protons from Ru to Zr (Ru/Zr) showing the difference of 10% in magnetic field strength.

### B. Azimuthal angle correlation between electromagnetic field and matter geometry

In this work we focus on taking into account the feedback effects from the electric and chiral magnetic conductivities and see their effects on the azimuthally fluctuating

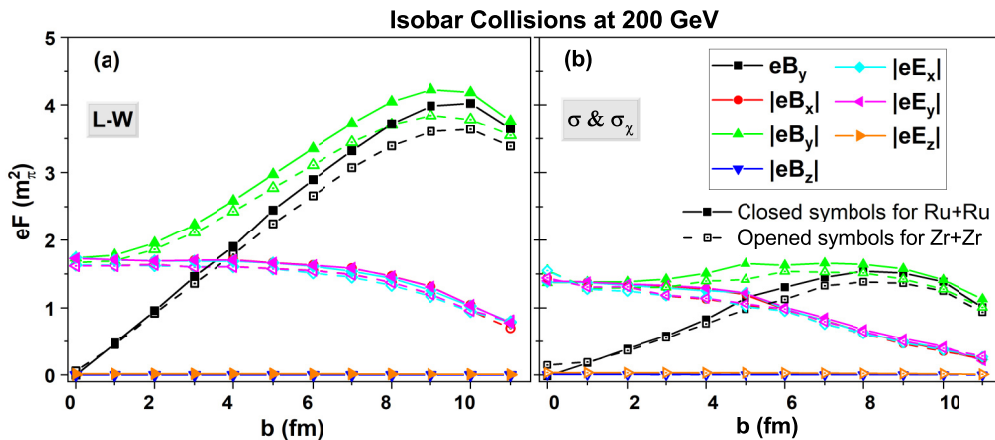


FIG. 5.  $e\mathbf{F}$  (in units of  $m_\pi^2$ ) in isobar collisions (halo-type) at  $\sqrt{s_{NN}} = 200$  GeV as a function of the impact parameter at  $t = 0$  fm/c for zero conductivity case and  $t = t_Q$  fm/c for finite conductivities case and compared between these two cases.

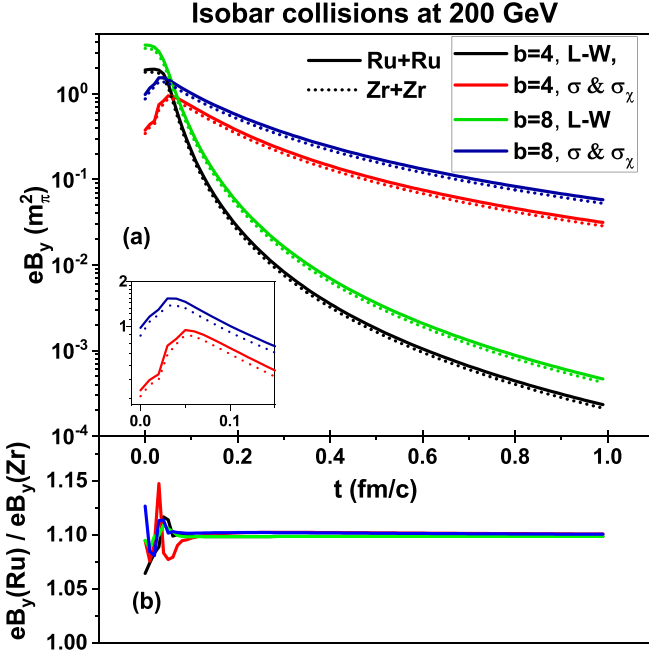


FIG. 6. Time evolution of the magnetic field  $eB_y$  in isobar collisions for  $b = 4, 8$  fm at  $\sqrt{s_{NN}} = 200$  GeV, compared between the zero-conductivity case and finite conductivities case at  $(0, 0, 0)$ .

directions of electric and magnetic field. The effect of finite conductivities on spatial distribution and time behavior of the electromagnetic field in isobar collisions have been discussed in the previous subsection, we further extend our investigation to the correlation between azimuthally fluctuating electromagnetic fields with matter geometry characterized by participant plane and also give their effects on EM field related observables. So in the following subsection we give our exploration for these correlations.

### 1. Magnetic field and participant plane

In this subsection we show the study of the correlation between azimuthal direction of the magnetic field ( $\Psi_B$ ) and participant plane ( $\Psi_2$ ). The correlations have been studied in the presence of finite conductivities and compared to the zero-conductivity system. Before we give numerical results it is important to mention that the electric and magnetic fields fluctuate strongly in azimuthal direction and magnitude on the event-by-event basis and so does the participant plane. It is important to take into account the orientation of  $\mathbf{B}$  field with the corresponding matter geometry on an event-by-event basis. Also the magnetic field induced effects which we observe occur along or perpendicular to the direction of magnetic field, so it is important to determine the direction of  $\mathbf{B}$  field in accordance with experiments. By studying the correlation between  $\Psi_B$  and  $\Psi_2$  we can determine the distribution of relative angle on event-by-event basis over many events and eventually we can give their effects on the CME observable. Here, we note that usually the participant plane  $\Psi_n$  is rotated by  $\pi/n$  as shown in Eq. (9) to serve as proxy for the event plane measured in experiments [59] and also a rotation is performed for the condition of sufficiently small elliptic flow

[60], however in our model we do not consider this rotation. In our study we focus on seeing the effect of finite  $\sigma$  and  $\sigma_\chi$  on the correlation between magnetic field and initial geometry of colliding system in Ru + Ru and Zr + Zr collisions.

In Fig. 7 we give the histograms of  $\Psi_B - \Psi_2$  on an event-by-event basis for Ru + Ru collisions [first row, i.e., Fig. 7(a)] and Zr + Zr collisions [second row, i.e., Fig. 7(b)] at  $\sqrt{s_{NN}} = 200$  GeV for  $b = 0, 4, 7, 10$  fm. In each row of the figure we compare histograms obtained from the zero-conductivity case to the finite conductivities case. We calculate the  $\Psi_B$  at  $\mathbf{r} = (0, 0, 0)$ , and  $t = 0$  fm/c for zero-conductivity case and  $t = t_Q$  fm/c for the finite conductivity case. The histograms given in Fig. 7(a) for Ru + Ru collisions at  $b = 0$  fm are almost uniform which represents that  $\Psi_B$  and  $\Psi_2$  are uncorrelated in fully overlapped collisions in both the vacuum and finite-conductivity cases. However, for  $b > 0$  fm as shown in the figure, for  $b = 4, 7, 10$  fm histograms show a certain correlation between  $\Psi_B$  and  $\Psi_2$  which have trends similar to Gaussian shape with wide widths and peaking at  $\pi/2$  for both the zero-conductivity and finite conductivities cases. The peak of the histogram for the zero-conductivity case is larger and its width is narrower as compared to the finite conductivity case. This difference of the peak and width is very minimal in peripheral collisions at  $b = 10$  fm as there are less numbers of participants at this impact parameter. The similar behavior is observed in Zr + Zr collisions as shown in Fig. 7(b). Figure 7 is for deformed nuclei parameters, we checked that halo-type nuclei parameters also have similar histograms.

Shown in Fig. 8 are the results for two-dimensional (2D) distribution plots of  $\Psi_B$  and  $\Psi_2$  for impact parameters  $b = 0, 4, 7, 10$  fm at  $\sqrt{s_{NN}} = 200$  GeV in Ru + Ru collisions. The scatter plots obtained in zero-conducting medium are presented in the first row [Fig. 8(a)], while the scatter plots obtained in the conducting medium case are presented in the second row [Fig. 8(b)]. Again for  $b = 0$  fm for both cases the distribution is uniform showing extremely weak correlation in fully overlapped collisions. However for  $b = 4, 7, 10$  fm the distribution of the scatter plot shows the concentration of distributions at  $(\Psi_B, \Psi_2) = (\pi/2, 0)$  indicating the existence of a correlation between two angles in both nonconducting and conducting media. We observed the spread in  $\Psi_B$  is thinner in finite conductivity case as compared to zero-conductivity case. We have also checked 2D scatter plots for Zr + Zr collisions and the behavior is similar to that found in Ru + Ru collisions. Our histogram results and scatter plots between  $\Psi_B$  and  $\Psi_2$  are similar to those reported in Refs. [33,43]. Figure 8 is for the deformed nuclei parameters, we checked that the halo-type nuclei parameters also have similar scatter plots.

Shown in Fig. 9 is the correlation between  $\Psi_B$  and  $\Psi_2$  in isobar collisions as a function of  $b$  in the first row ( $N_{\text{part}}$  in the second row) and compared the correlation between zero-conductivity and finite conductivities cases. Results with solid symbol with solid lines are from halo-type nuclei while open symbols with dotted lines are from deformed nuclei parameters. There is a small difference found for both parameter settings which can also be seen from the relative ratios in Fig. 9(b). From the figure we can also see that the correlation  $\langle \cos 2(\Psi_B - \Psi_2) \rangle$  depends on centrality. Since spatial distribution of the magnetic fields are symmetric around the  $x = 0$

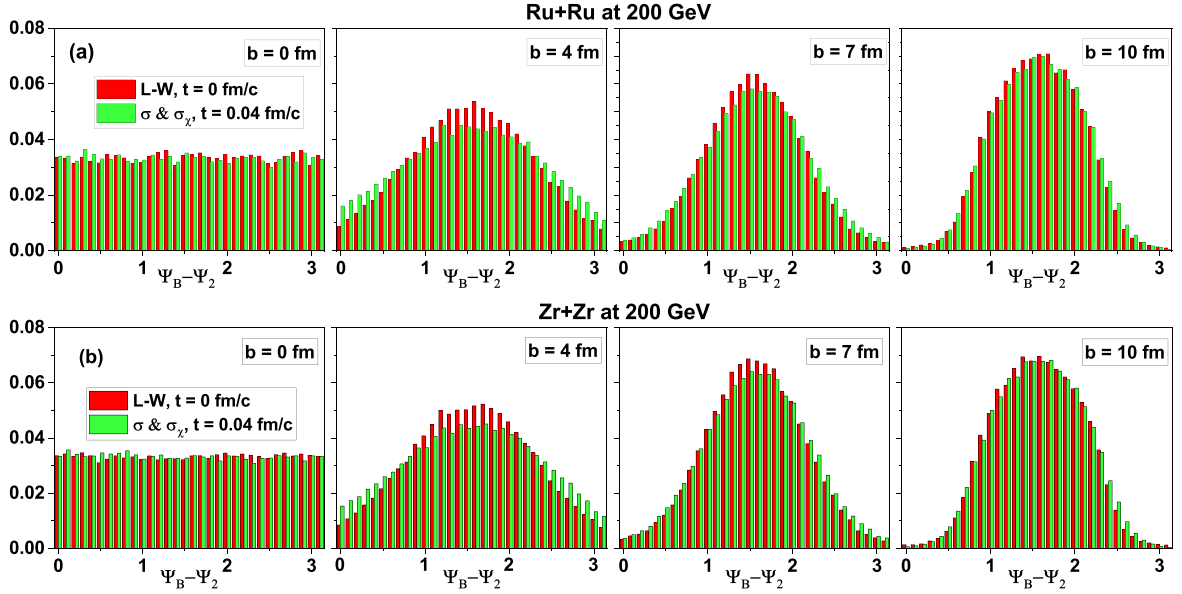


FIG. 7. The histograms of  $\Psi_B - \Psi_2$  on event-by-event basis and compared between vacuum case (L-W) and finite conductivity case for impact parameter  $b = 0, 4, 7, 10$  at  $\mathbf{r} = (0, 0, 0)$ . Histogram results for Ru + Ru collisions are in the first row and for Zr + Zr collisions are in the second row at  $\sqrt{s_{NN}} = 200$  GeV.

axis but asymmetric around the  $y = 0$  axis in the presence of finite conductivities, we observe their effects on correlation as well on the transverse plane. On a whole, results are consistent with the histograms and scatter plots given in Figs. 7 and 8, that is, for a small impact parameter and very large impact parameter the correlation is almost zero and very weak in the zero-conductivity and finite conductivities cases. However, from the figure we also see that at approximately  $b = 7-9$  fm,

the correlations  $\langle \cos 2(\Psi_B - \Psi_2) \rangle$  reach their maximum value about  $-0.55$  for the vacuum case but the maximum value for the finite conductivities case is smaller. From the figure we also see that taking into account finite  $\sigma$  and  $\sigma_\chi$  results are quantitatively different in magnitudes of correlation as compared to the vacuum case but qualitatively consistent with the vacuum case. The results for the vacuum case are almost similar to those given in Ref. [43]. Quantitatively the cor-

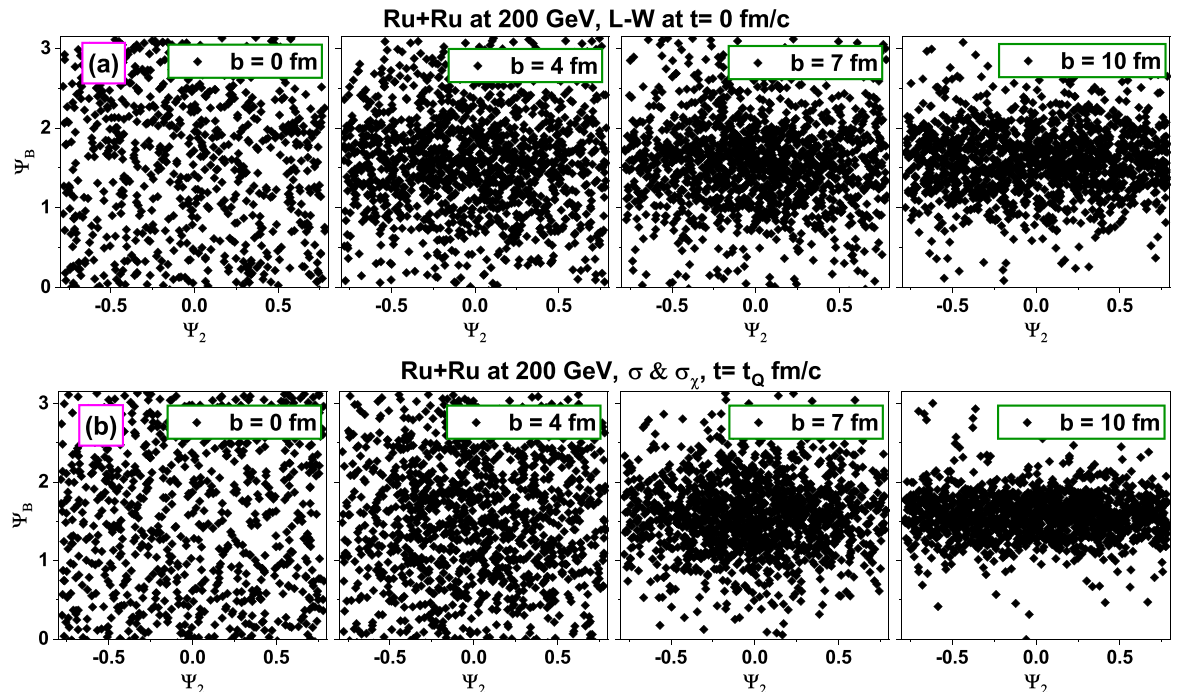


FIG. 8. The scatter plots on  $\Psi_B - \Psi_2$  plane in Ru + Ru collisions at  $\sqrt{s_{NN}} = 200$  GeV for impact parameters  $b = 0, 4, 7, 10$  fm, compared between zero-conductivity case (first row) and finite conductivities case (second row).



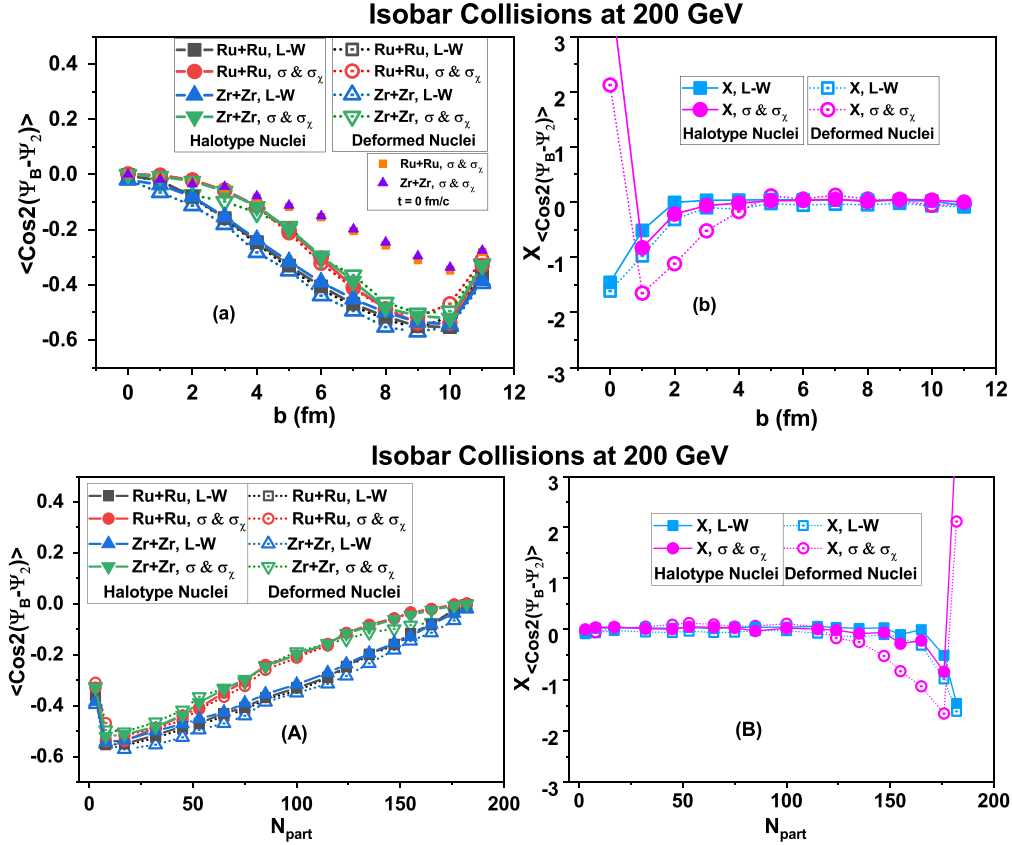


FIG. 9. The correlation  $\langle \cos 2(\Psi_B - \Psi_2) \rangle$  as a function of impact parameter  $b$  in the first row ( $N_{\text{part}}$  in the second row) in transverse plane, respectively, and their relative ratios in isobar collisions at  $\sqrt{s_{NN}} = 200$  GeV, compared between the zero-conductivity case ( $t = 0$  fm/c) and finite conductivities case ( $t = t_0$ ). Orange and purple symbols in (a) are for the finite conductivity case at  $t = 0$  fm/c.

relation at  $(0, 0, 0)$  is suppressed to 40% in the presence of finite  $\sigma$  and  $\sigma_\chi$  in intermediate impact parameter (at  $b = 5$  fm) but this suppression decreases with the increasing impact parameter (suppression of 9% at  $b = 10$  fm) for both Ru + Ru and Zr + Zr collisions. The relative ratio at the origin point has similar trends for both cases but the conducting medium case shows larger deviation from zero at smaller centralities. We note that we have compared the results at the time  $t = t_0$  fm/c because we observed a maximum value for the magnetic field at this time for the finite conductivities case, however we have also checked that if we take earlier time or later time then the magnitude of the correlation is smaller. Correlation for finite conductivity case at  $t = 0$  fm/c is also shown by orange and magenta solid symbols in Fig. 9(a) where we can see that at  $t = 0$  fm/c the correlation for the finite conductivity case is much smaller than the vacuum case.

According to the magnetic field induced effects, they show a directly proportional correlation with  $eB^2$  along with  $\langle \cos 2(\Psi_B - \Psi_2) \rangle$ . The correlator  $\langle eB^2 \cos 2(\Psi_B - \Psi_2) \rangle$  quantifies the effectiveness of the magnetic field induced effects such as generating a CME signal in the  $\gamma$  correlator [33,34]. So in Fig. 10 we show the results for  $\langle eB^2 \cos 2(\Psi_B - \Psi_2) \rangle$  in Ru + Ru and Zr + Zr collisions as a function of impact parameter  $b$  in the first row ( $N_{\text{part}}$  in the second row) for vacuum scenario compared to the finite  $\sigma$  and  $\sigma_\chi$  scenario. Results with solid symbols with solid lines represents for

halo-type nuclei settings while open symbols with dashed lines represent deformed nuclei settings. Comparing with Figs. 5 and 9 one can see that it inherits influence from both magnetic field and correlation. We see that by considering finite  $\sigma$  and  $\sigma_\chi$  the magnitude is decreased 6 times but qualitatively the behavior is similar to the vacuum case. We also see that maximum values of  $\langle eB^2 \cos 2(\Psi_B - \Psi_2) \rangle$  are observed at earlier centrality in case of conductivities. The sizable suppression can be observed for isobar collisions when compared to the  $\sigma = \sigma_\chi = 0$  case. We have also compared the relative ratios in two different scenarios and we found that although two scenarios differ quantitatively, qualitative trends are similar for  $b > 4$  fm. From the results presented in Fig. 10, we can see that magnetic field in two different scenarios can play an important role to the charge azimuthal correlation  $\Delta\gamma$  as well according to Eq. (1). Our study suggests that taking into account the feedback effects from QGP properties such finite conductivities can also suppress the magnetic field induced effects such as CME signal. So when calculating the charge azimuthal correlation it is important to incorporate QGP properties such as  $\sigma$  and  $\sigma_\chi$ .

## 2. Time-averaged correlation

In the previous subsection we have provided a comparison of the correlators at fixed time for the zero-conductivity case

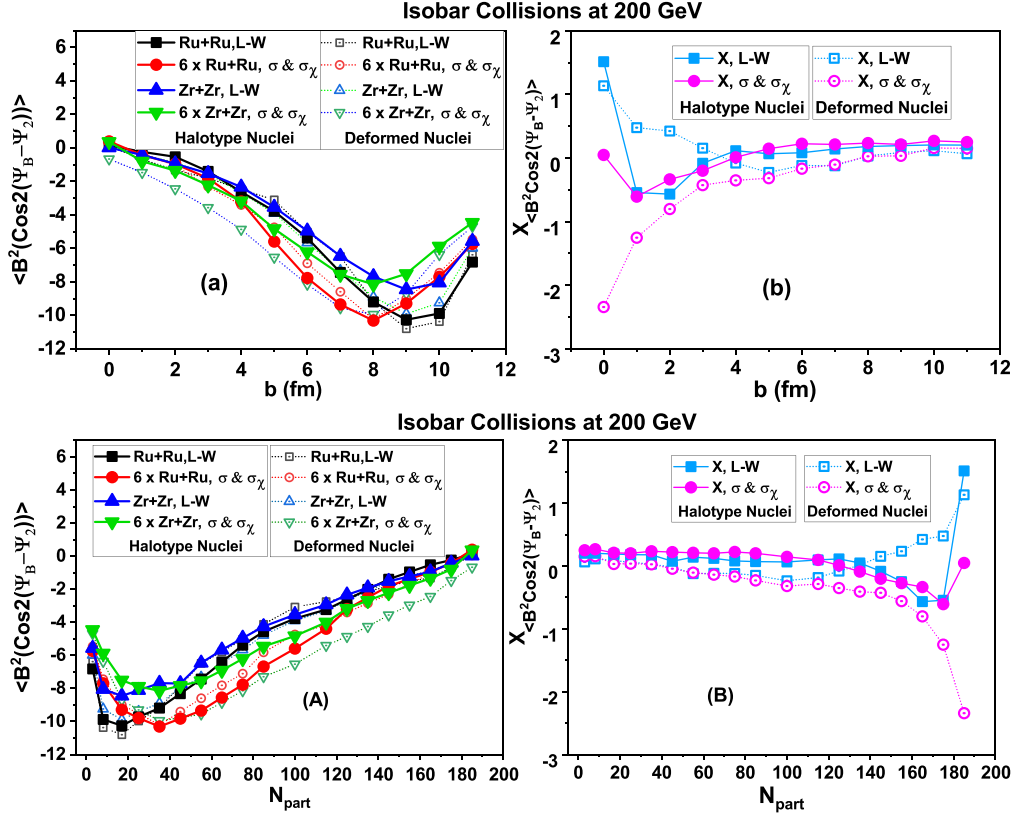


FIG. 10. The correlation  $\langle eB^2 \cos 2(\Psi_B - \Psi_2) \rangle$  as a function of impact parameter  $b$  in first row ( $N_{\text{part}}$  second row) in the transverse plane and their relative ratios, respectively, in isobar collisions at  $\sqrt{s_{NN}} = 200$  GeV, compared between the zero-conductivity case ( $t = 0$  fm/c) and finite conductivities case ( $t = t_Q$ ).

( $t = 0$  fm/c) and finite conductivity case ( $t = t_Q$ ). Since, EM fields behavior varies with respect to both time and space, so their impact on physical observables should be at average level in the lifespan of quark and nuclear matter. To quantify the average effects of correlators on physical observables we define time-averaged correlators as

$$\langle \mathbf{G} \rangle_t(x) \equiv \frac{\int dt \mathbf{G}(t, x)}{\int dt}, \quad (11)$$

where  $\mathbf{G}$  represents correlator  $\langle \cos 2(\Psi_F - \Psi_2) \rangle_t$  or  $\langle e\mathbf{F}^2 \cos 2(\Psi_F - \Psi_2) \rangle_t$  with  $\mathbf{F}$  being a magnetic or electric field. For numerical calculation we discretize the whole time period with discrete time points  $t_i$  and evaluate corresponding  $\mathbf{G}(t_i, x)$ , so the above equation can be written into the iterative form as

$$\langle \mathbf{G} \rangle_t(x) \equiv \frac{\sum_i \mathbf{G}(t_i, x) \Delta t_i}{\sum_i \Delta t_i}, \quad (12)$$

where  $\Delta t$  is time interval and we choose  $\Delta t = 0.02$  fm/c for our simulation. Several studies have shown that without considering the characteristics of the medium, the maximum magnetic field occurs in the geometric center shortly after the collision and then the magnetic field rapidly decays with time as  $t^{-3}$  in the early phase of the evolving matter [1–4,33,61]. However, considering the medium feedback, such as conductivities, the decay of the magnetic field is significantly slowed down, for example, for ideal magnetohydrodynamics with

infinite electric conductivity the magnetic field decay with time as  $t^{-1}$  [62–64]. Similar behavior is also observed and shown in Fig. 6 for decay of the magnetic field with and without taking into account medium feedback. Also we see in Fig. 6 that for time interval  $0 \rightarrow 1$  fm/c the magnetic field magnitude becomes much smaller at  $t = 1$  fm/c than the maximum values for magnetic fields observed soon after the collision time. However in this study for time-averaged correlations we have considered a longer time interval, i.e.,  $0 \rightarrow 2$  fm/c. It is shown in the previous subsection that halo-type nuclei and deformed nuclei structures have almost similar results for the correlators, so in this subsection we only give results for the halo-type nuclei structure of Ru and Zr nuclei.

In Fig. 11, we give the time-averaged correlation  $\langle \cos 2(\Psi_B - \Psi_2) \rangle_t$  as a function of impact parameter  $b$  fm. From the figure we can also see that time-averaged correlation depends on different centralities. Time-averaged correlations for the zero conductivity case and finite conductivity case show similar behaviors, however, for the finite conductivities case the magnitudes are a little smaller than the zero conductivity case. From the figure we see that for  $b = 0$  fm the time averaged correlation is almost zero which is consistent to the histogram for  $b = 0$  fm. The time-averaged correlation increases with an increase in impact parameter until it reaches a maximum value for  $b = 7-9$  fm, and then it decreases again for a very large impact parameter. Relative ratios shown in Fig. 11(b) have similar trends for the zero conductivity case

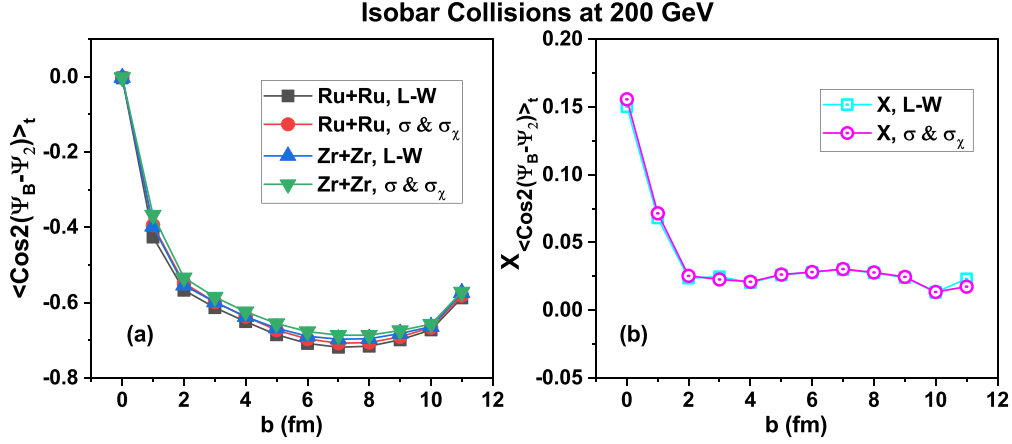


FIG. 11. The time-averaged correlation  $\langle \cos 2(\Psi_B - \Psi_2) \rangle_t$  as a function of impact parameter  $b$  (fm) in transverse plane and their relative ratios, respectively, in isobar collisions at  $\sqrt{s_{NN}} = 200$  GeV, comparison between the zero-conductivity case and finite conductivities case is presented.

and finite conductivities case. From the figure, we see a small difference in magnitude of time-averaged correlation when taking into account finite  $\sigma$  and  $\sigma_\chi$ , and also qualitative behavior is consistent with the vacuum case.

In Fig. 12, we show time-averaged correlation  $\langle e\mathbf{B}^2 \cos 2(\Psi_B - \Psi_2) \rangle_t$  as a function of impact parameter  $b$  fm. We show the results for Ru + Ru and Zr + Zr collisions for the vacuum scenario compared to the finite  $\sigma$  and  $\sigma_\chi$  scenario. The results show that they inherit influence from both the squared magnetic field as well as from the correlation  $\cos 2(\Psi_B - \Psi_2)$  on a time averaged level. We also see that for time interval 0–2 fm/c the time-averaged correlation in the presence of finite  $\sigma$  and  $\sigma_\chi$  is roughly 2.5 times smaller than the time-averaged correlation for the zero-conductivity case. Although the magnetic field in the presence of conductivities has a larger magnitude at later times of evolution when compared with the zero conductivity case but the interplay between squared magnetic field  $e\mathbf{B}^2$  and correlation  $\cos 2(\Psi_B - \Psi_2)$  becomes smaller when taking the time-average in intervals. Also

at initial time  $\langle e\mathbf{B}^2 \cos 2(\Psi_B - \Psi_2) \rangle$  is much larger than the finite conductivity case so even after calculating the time-averaged correlation the magnitude stays larger. On a whole, qualitative behavior for time-averaged correlation is similar to that observed in Fig. 10. The time-averaged correlation  $\langle e\mathbf{B}^2 \cos 2(\Psi_B - \Psi_2) \rangle_t$  also suggests that by taking into account the medium feedback effects from QGP properties such finite conductivities can also suppress the magnetic field induced effects such as CME effects.

### 3. Electric field and participant plane

In this subsection we give the brief study of the correlation between azimuthal direction of the electric field ( $\Psi_E$ ) and participant plane ( $\Psi_2$ ) for completeness. As we have noticed in Fig. 5 that the electric field can also be comparably strong with the magnetic field. Possible charge distribution induced by a strong electric field is an example of this. Similar to the magnetic field, we study the correlation  $\langle \cos 2(\Psi_E - \Psi_2) \rangle$ . In Fig. 13, we show the results as a function of  $b$  ( $N_{part}$ ) in Ru + Ru and Zr + Zr collisions at  $\sqrt{s_{NN}} = 200$  GeV for

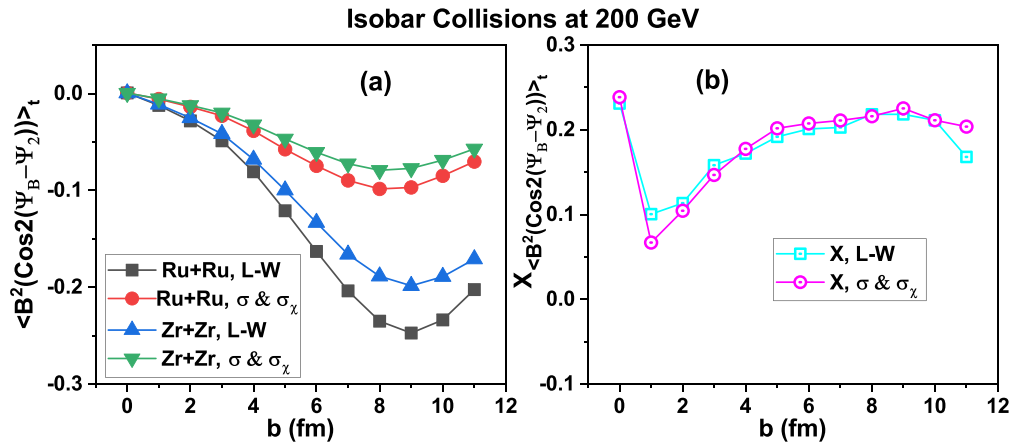


FIG. 12. The time-averaged correlation  $\langle e\mathbf{B}^2 \cos 2(\Psi_B - \Psi_2) \rangle_t$  as a function of impact parameter  $b$  (fm) in transverse plane and their relative ratios in isobar collisions at  $\sqrt{s_{NN}} = 200$  GeV, comparison between the zero-conductivity case and finite conductivities case is presented.

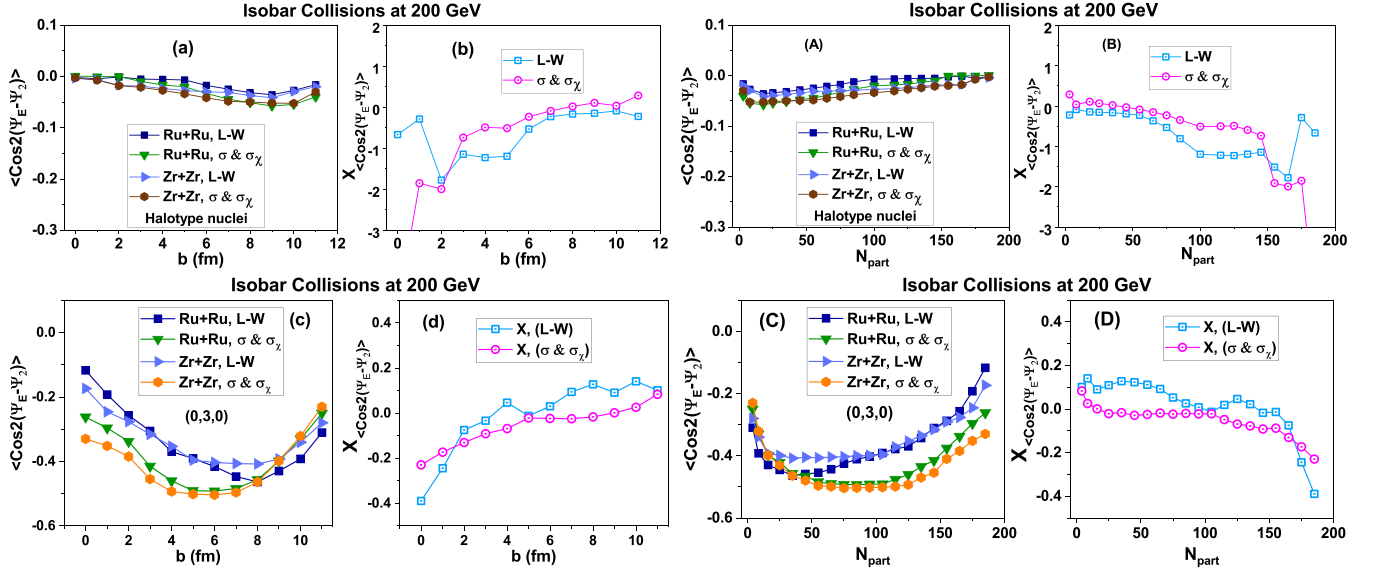


FIG. 13. The correlation  $\langle \cos 2(\Psi_E - \Psi_2) \rangle$  as a function of impact parameter  $b$  at two different positions in transverse plane that is  $\mathbf{r} = (0, 0, 0)$  and  $\mathbf{r} = (0, 3, 0)$  in first and second rows, respectively, and their relative ratios in isobar collisions at  $\sqrt{s_{NN}} = 200$  GeV, comparison between the zero-conductivity case ( $t = 0$  fm/c) and finite conductivities case ( $t = t_Q$ ) is presented.

vacuum and conducting medium cases at points  $(0, 0, 0)$  in the first row and  $(0, 3, 0)$  in the second row. As we noticed in a previous section that halo-type and deformed nuclei parameters have little difference on correlations and their relative ratios in our setup so in the first row of Fig. 13 results are obtained by using halo-type nuclei parameters and results in the second row are obtained by using deformed nuclei parameters. In Fig. 13(a), we calculate  $\langle \cos 2(\Psi_E - \Psi_2) \rangle$  as a function of  $b$  and we can see that the correlation is very weak for Ru + Ru and Zr + Zr collisions for all impact parameters. The relative ratios shown in Fig. 13(b) for both vacuum and medium case have similar trends for  $b > 3$  fm ( $N_{part} < 160$ ). However, this weak correlation can be understood together with the spatial distributions of electric field components given in Fig. 3, where we can see that at  $(0, 0, 0)$  the electric field is very weak. The results shown in the second row of Fig. 13, which corresponds to point  $(0, 3, 0)$ , show the sizable correlation for the zero-conductivity limit and finite conductivities case. We also observe enhancement of correlation in the presence of finite  $\sigma$  and  $\sigma_\chi$  for small centralities. The relative ratios measured at this point for the two cases have shown similar trends for centrality dependence. So, we see that two scenarios behave similarly qualitatively but differ in magnitude quantitatively.

Similar to the magnetic field, the possible observable quantity related to the electric field can also be proportional to  $e\mathbf{E}^2$  and  $\langle \cos 2(\Psi_E - \Psi_2) \rangle$  so, in Fig. 14, we calculate the correlation  $\langle e\mathbf{E}^2 \cos 2(\Psi_E - \Psi_2) \rangle$  as function of  $b$  ( $N_{part}$ ) for Ru + Ru and Zr + Zr collisions at  $\sqrt{s_{NN}} = 200$  GeV. We compared the results for the vacuum case with the finite conductivities case at point  $(0, 0, 0)$  in the first row and at point  $(0, 3, 0)$  in the second row of the figure. We see that it is very weak at  $(0, 0, 0)$  because the strength of the electric field is also very weak at the origin point. The relative ratio at this point shows qualitatively almost similar trend for  $b$  fm ( $N_{part}$ ) dependence. However, we notice an observable effect

at point  $(0, 3, 0)$  which can be understood together with the spatial distribution and the electric field at this point. From the figure we also notice that the introduction of finite  $\sigma$  and  $\sigma_\chi$  in a system do affect the strength (4 times smaller) of correlation quantitatively, however the qualitative picture is somewhat similar to the vacuum case. Relative ratios show different behavior at  $(0, 3, 0)$ , for the case of finite conductivities relative ratios are near zero, however for cases of zero conductivity the relative ratio differs from zero. The results shown in the figure suggest that while calculating an observable quantity related to the electric field, it is important to take into account feedback effects from the medium properties.

#### IV. SUMMARY AND OUTLOOK

In this study, we have conducted a systematic investigation on the effects of electric ( $\sigma$ ) and chiral magnetic ( $\sigma_\chi$ ) conductivities on the impact parameter and space-time behaviors of the electromagnetic fields generated in high-energy isobar collisions. Our results show that in the transverse plane partially broken symmetry is observed for the electric and magnetic fields in isobar collisions in the presence of finite  $\sigma$  and  $\sigma_\chi$ , consistent with those observed in Au + Au collisions. Although the magnitude is smaller for the case of a conducting medium at earlier time but the lifetime of fields is much longer when compared to the zero-conductivity limit (Lienard-Wiechert). We also confirm that the magnetic fields differ by 10% even in the case of finite conductivities.

We also performed a detailed study on the azimuthal fluctuation of electromagnetic fields ( $e\mathbf{F}$ ) in the presence of conductivities and studied their correlations with initial matter geometry, i.e.,  $\langle \cos 2(\Psi_F - \Psi_2) \rangle$  and  $\langle e\mathbf{F}^2 \cos 2(\Psi_F - \Psi_2) \rangle$  on an event-by-event basis. Comparison of the correlations has been presented between the vacuum (L-W) and finite conductivities cases in this study. We see a sizable suppression of



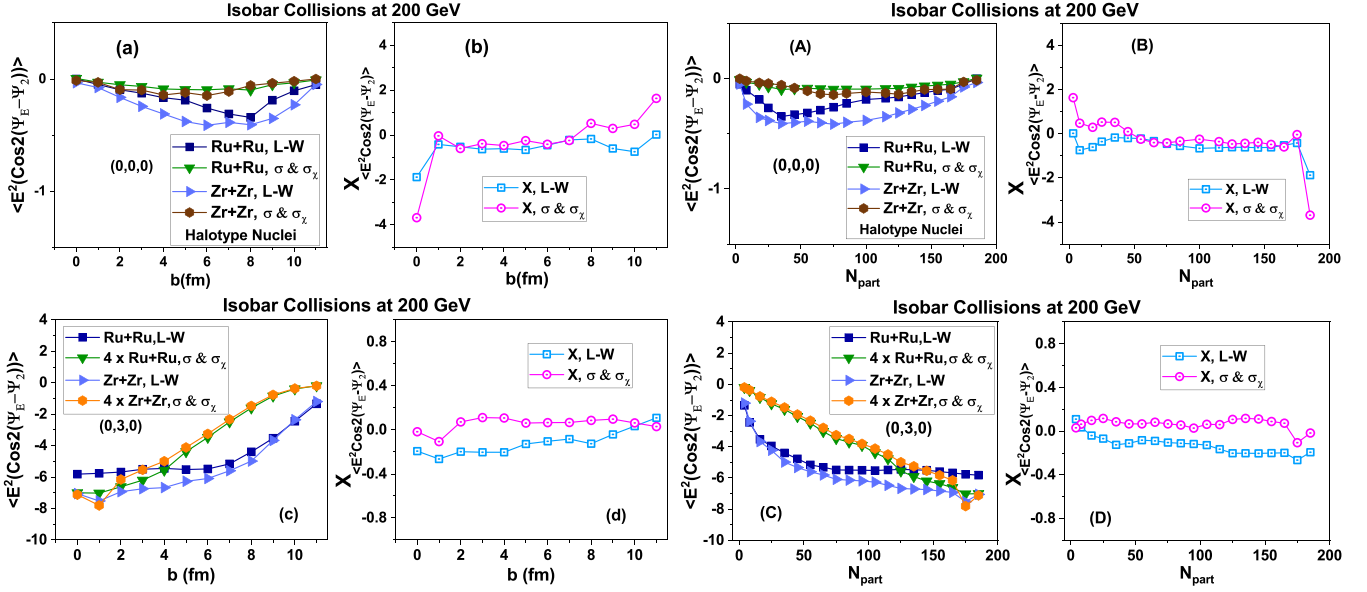


FIG. 14. The correlation  $\langle eE^2 \cos 2(\Psi_E - \Psi_2) \rangle$  as a function of impact parameter  $b$  at two different positions in transverse plane that is  $r = (0, 0, 0)$  and  $r = (0, 3, 0)$  in first and second rows, respectively, and their relative ratios in isobar collisions at  $\sqrt{s_{NN}} = 200$  GeV, compared with the zero-conductivity case ( $t = 0$  fm/ $t = 0$  fm/c) and finite conductivities case ( $t = t_Q$ ).

the correlations for fixed time and time-averaged correlations in the presence of conducting medium, which reflects the importance of taking into account the medium properties such as conductivities while calculating the experimentally measurable observable such as  $\Delta\gamma$  because quantities related to EM fields inherit influence from both the strength and the correlation between EM field direction and initial geometry. While the relative ratios measured in this paper show similar trends for centrality dependence, large deviations are observed from central to midcentral collisions. We also take into account the two different WS nuclei parameters, namely, deformed nuclei and halo-type nuclei and although they show a difference in results, our calculation shows that the difference is not large and also qualitative behavior studied by relative ratios is similar for large centralities.

While in this work we have provided a quantitative understanding of the influence of finite  $\sigma$  and  $\sigma_\chi$  on the electromagnetic fields as well as their azimuthal direction correlation with the initial geometry characterized by the participant plane in isobar collisions, it can be improved in several directions. It is needful to integrate these electromagnetic fields into a transport model or hydrodynamic model,

from which one may draw a more solid conclusion about the consequent effects. In this study, we have only considered finite values for  $\sigma$  and  $\sigma_\chi$ , but the values should change with the dynamical expansion in QGP. While in this work we only considered the participant plane one may also consider the spectator plane to see their correlation in the presence of conductivities. In the future, it will be interesting to study the correlation between the fluctuations of electromagnetic anomaly ( $\mathbf{E} \cdot \mathbf{B}$ ) and  $n$ th harmonic participant (or spectator) plane in the presence of conductivities. In an upcoming effort, we will extend our studies to these directions.

## ACKNOWLEDGMENTS

We are grateful to University of Chinese Academy of Sciences for providing a platform to carry out simulations. Thanks to X. G. Huang and G. L. Ma for discussions during the conference Chirality, Vorticity and Magnetic Field 2023. Thanks to Q. Wang, H. Mei, S. S. Cao, X. L. Sheng, D. Jian, H. Xu, and A. Huang for helpful discussions. This work is supported by the Ministry of Science and Technology (MOST) of China under Grant No. QN2023205001L and RFIS-NSFC under Grant No. 12350410364.

[1] A. Bzdak and V. Skokov, *Phys. Lett. B* **710**, 171 (2012).  
 [2] W.-T. Deng and X.-G. Huang, *Phys. Rev. C* **85**, 044907 (2012).  
 [3] V. Voronyuk, V. D. Toneev, W. Cassing, E. L. Bratkovskaya, V. P. Konchakovski, and S. A. Voloshin, *Phys. Rev. C* **83**, 054911 (2011).  
 [4] V. Skokov, A. Y. Illarionov, and V. Toneev, *Int. J. Mod. Phys. A* **24**, 5925 (2009).  
 [5] Y. Zhong, C.-B. Yang, X. Cai, and S.-Q. Feng, *Adv. High Energy Phys.* **2014**, 193039 (2014).

[6] D. E. Kharzeev, L. D. McLerran, and H. J. Warringa, *Nucl. Phys. A* **803**, 227 (2008).  
 [7] D. Kharzeev and A. Zhitnitsky, *Nucl. Phys. A* **797**, 67 (2007).  
 [8] K. Fukushima, D. E. Kharzeev, and H. J. Warringa, *Phys. Rev. D* **78**, 074033 (2008).  
 [9] K. Fukushima, D. E. Kharzeev, and H. J. Warringa, *Phys. Rev. Lett.* **104**, 212001 (2010).  
 [10] D. E. Kharzeev and D. T. Son, *Phys. Rev. Lett.* **106**, 062301 (2011).

- [11] D. T. Son and P. Surowka, *Phys. Rev. Lett.* **103**, 191601 (2009).
- [12] D. T. Son and A. R. Zhitnitsky, *Phys. Rev. D* **70**, 074018 (2004).
- [13] M. A. Metlitski and A. R. Zhitnitsky, *Phys. Rev. D* **72**, 045011 (2005).
- [14] D. E. Kharzeev and H.-U. Yee, *Phys. Rev. D* **83**, 085007 (2011).
- [15] Y. Burnier, D. E. Kharzeev, J. Liao, and H.-U. Yee, *Phys. Rev. Lett.* **107**, 052303 (2011).
- [16] Y. Burnier, D. E. Kharzeev, J. Liao, and H. U. Yee, *arXiv:1208.2537* (2012).
- [17] H.-U. Yee and Y. Yin, *Phys. Rev. C* **89**, 044909 (2014).
- [18] Y. Jiang, X.-G. Huang, and J. Liao, *Phys. Rev. D* **92**, 071501(R) (2015).
- [19] B. I. Abelev *et al.* (STAR Collaboration), *Phys. Rev. Lett.* **103**, 251601 (2009).
- [20] B. I. Abelev *et al.* (STAR Collaboration), *Phys. Rev. C* **81**, 054908 (2010).
- [21] B. Abelev *et al.* (ALICE Collaboration), *Phys. Rev. Lett.* **110**, 012301 (2013).
- [22] L. Adamczyk *et al.* (STAR Collaboration), *Phys. Rev. C* **88**, 064911 (2013).
- [23] L. Adamczyk *et al.* (STAR Collaboration), *Phys. Rev. Lett.* **113**, 052302 (2014).
- [24] L. Adamczyk *et al.* (STAR Collaboration), *Phys. Rev. C* **89**, 044908 (2014).
- [25] V. Khachatryan *et al.* (CMS Collaboration), *Phys. Rev. Lett.* **118**, 122301 (2017).
- [26] S. Schlichting and S. Pratt, *Phys. Rev. C* **83**, 014913 (2011).
- [27] F. Wang and J. Zhao, *Phys. Rev. C* **95**, 051901(R) (2017).
- [28] J. Zhao (STAR Collaboration), *Nucl. Phys. A* **982**, 535 (2019).
- [29] A. Bzdak, V. Koch, and J. Liao, *Lect. Notes Phys.* **871**, 503 (2013).
- [30] J. Zhao, H. Li, and F. Wang, *Eur. Phys. J. C* **79**, 168 (2019).
- [31] H.-J. Xu *et al.*, *Chin. Phys. C* **42**, 084103 (2018).
- [32] F. Wang, *Phys. Rev. C* **81**, 064902 (2010).
- [33] J. Błoczynski, X.-G. Huang, X. Zhang, and J. Liao, *Phys. Lett. B* **718**, 1529 (2013).
- [34] J. Błoczynski, X.-G. Huang, X. Zhang, and J. Liao, *Nucl. Phys. A* **939**, 85 (2015).
- [35] S. Chatterjee and P. Tribedy, *Phys. Rev. C* **92**, 011902(R) (2015).
- [36] S. A. Voloshin, *Phys. Rev. Lett.* **105**, 172301 (2010).
- [37] M. Abdallah *et al.* (STAR Collaboration), *Phys. Rev. C* **105**, 014901 (2022).
- [38] Y. Hu (STAR Collaboration), *EPJ Web Conf.* **259**, 13013 (2022).
- [39] Y. Hu (STAR Collaboration), *Acta Phys. Polon. Supp.* **16**, 44 (2023).
- [40] W.-T. Deng, X.-G. Huang, G.-L. Ma, and G. Wang, *Phys. Rev. C* **94**, 041901(R) (2016).
- [41] W. T. Deng, X. G. Huang, G. L. Ma, and G. Wang, *Phys. Rev. C* **97**, 044901 (2018).
- [42] S. Shi, H. Zhang, D. Hou, and J. Liao, *Nucl. Phys. A* **982**, 539 (2019).
- [43] X.-L. Zhao, G.-L. Ma, and Y.-G. Ma, *Phys. Rev. C* **99**, 034903 (2019).
- [44] L. McLerran and V. Skokov, *Nucl. Phys. A* **929**, 184 (2014).
- [45] K. Tuchin, *Phys. Rev. C* **88**, 024911 (2013).
- [46] K. Tuchin, *Phys. Rev. C* **91**, 064902 (2015).
- [47] H. Li, X.-L. Sheng, and Q. Wang, *Phys. Rev. C* **94**, 044903 (2016).
- [48] I. Siddique, X.-L. Sheng, and Q. Wang, *Phys. Rev. C* **104**, 034907 (2021).
- [49] I. Siddique, S. Cao, U. Tabassam, M. Saeed, and M. Waqas, *Phys. Rev. C* **105**, 054909 (2022).
- [50] C. Loizides, J. Nagle, and P. Steinberg, *SoftwareX* **1–2**, 13 (2015).
- [51] B. Alver *et al.* (PHOBOS Collaboration), *Phys. Rev. Lett.* **98**, 242302 (2007).
- [52] M. L. Miller, K. Reygers, S. J. Sanders, and P. Steinberg, *Annu. Rev. Nucl. Part. Sci.* **57**, 205 (2007).
- [53] B. Alver *et al.*, *Phys. Rev. C* **77**, 014906 (2008).
- [54] P. Moller, J. R. Nix, W. D. Myers, and W. J. Swiatecki, *At. Data Nucl. Data Tables* **59**, 185 (1995).
- [55] B. Pritychenko, M. Birch, B. Singh, and M. Horoi, *At. Data Nucl. Data Tables* **107**, 1 (2016); **114**, 371(E) (2017).
- [56] Q. Y. Shou *et al.*, *Phys. Lett. B* **749**, 215 (2015).
- [57] H.-j. Xu, H. Li, X. Wang, C. Shen, and F. Wang, *Phys. Lett. B* **819**, 136453 (2021).
- [58] X.-L. Zhao and G.-L. Ma, *Phys. Rev. C* **106**, 034909 (2022).
- [59] G.-Y. Qin, H. Petersen, S. A. Bass, and B. Muller, *Phys. Rev. C* **82**, 064903 (2010).
- [60] D. Teaney and L. Yan, *Phys. Rev. C* **83**, 064904 (2011).
- [61] K. Hattori and X. G. Huang, *Nucl. Sci. Tech.* **28**, 26 (2017).
- [62] V. Roy, S. Pu, L. Rezzolla, and D. Rischke, *Phys. Lett. B* **750**, 45 (2015).
- [63] S. Pu, V. Roy, L. Rezzolla, and D. H. Rischke, *Phys. Rev. D* **93**, 074022 (2016).
- [64] L. Yan and X. G. Huang, *Phys. Rev. D* **107**, 094028 (2023).